Intraseasonal oscillations of the Silk Road pattern lead to predictability in East Asian precipitation patterns and the Mei Yu front

ENVIRONMENTAL RESEARCH
COMMUNICATIONS

PAPER • OPEN ACCESS

Intraseasonal oscillations of the Silk Road pattern lead to predictability in East Asian precipitation patterns and the Mei Yu front

To cite this article: Mark R Muetzelfeldt *et al* 2023 *Environ. Res. Commun.* **5** 015003

Environmental Research Communications

PAPER

Intraseasonal oscillations of the Silk Road pattern lead to predictability in East Asian precipitation patterns and the Mei Yu front

Mark R Muetzelfeldt[1,4], **Reinhard Schiemann**[1], **Andrew G Turner**[1,2], **Pier Luigi Vidale**[1] and **Arathy Menon**[3]

[1] National Centre for Atmospheric Science, University of Reading, Reading, Berkshire, RG6 6BB, United Kingdom
[2] Department of Meteorology, University of Reading, Reading, Berkshire, RG6 6BB, United Kingdom
[3] Met Office, FitzRoy Road, Exeter, Devon, EX1 3 PB, United Kingdom
[4] Mark Muetzelfeldt, Department of Meteorology, University of Reading, Reading, Berkshire, RG6 6BB, UK.

E-mail: mark.muetzelfeldt@reading.ac.uk

Keywords: Silk Road pattern, East Asian precipitation, subtropical westerly jet, Mei Yu front, circumglobal teleconnection

OPEN ACCESS

RECEIVED
7 October 2022

REVISED
16 December 2022

ACCEPTED FOR PUBLICATION
4 January 2023

PUBLISHED
18 January 2023

Abstract

The Silk Road pattern (SRP) is analysed on intraseasonal timescales over summer using empirical orthogonal functions (EOFs) of the meridional wind at 200 hPa. The first two principal components explain almost equal amounts of variance, hence both are required to represent the intraseasonal SRP. The associated spatial loadings are 90° out of phase with each other, providing evidence that propagating oscillations are a natural mode of variability of the intraseasonal SRP. This is supported by Hovmöller diagrams of the meridional wind at 200 hPa and by phase diagrams of the first two EOFs, which both show a predominantly eastward-propagating oscillation. The oscillations are identified as plausibly being Rossby waves by means of waveguide theory. The subtropical westerly jet and East Asian rainfall patterns are found to be dependent on the phase of the oscillation: wet anomalies occur to the east of troughs in the jet, which are also regions where local jet entrances cause upper-level divergence via an ageostrophic circulation. Dry anomalies occur to the west of troughs, which are regions of upper-level convergence. The time-delayed location of the summer Mei Yu front relative to its climatology is dependent on the phase of the oscillation: when there is an upper-level trough located over the Korean Peninsula, the Mei Yu front is likely to be located further north than normal 3–8 days later, before returning to its climatological position. This suggests that the phase of the intraseasonal SRP acts as a potential source of predictability of the location of the Mei Yu front, which might allow for better prediction of the associated rains.

1. Introduction

The Silk Road pattern (SRP) is a large-scale summertime teleconnection of the upper-level winds over Europe and Asia (Enomoto *et al* 2003). It is a manifestation of the Rossby waves that form in the subtropical westerly jet (SWJ), where the SWJ acts as a waveguide due to the meridional change in zonal winds (Hoskins and Karoly 1981, Enomoto *et al* 2003, Stephan *et al* 2018). It can be considered as the Asian branch of the circumglobal teleconnection (Ding and Wang 2005). On seasonal timescales, it has been shown to have an effect on rainfall patterns over Asia (Wang *et al* 2017, Stephan *et al* 2018).

The SRP is commonly studied using empirical orthogonal function (EOF) analysis, in which the EOFs are calculated using the meridional winds at 200 hPa, as these capture the Rossby wave motion. The EOF analysis is normally performed on monthly (e.g. Yasui and Watanabe 2010) or seasonal (e.g. Stephan *et al* 2019) timescales, in which the purpose is to determine the activity of the SRP over a given summer season and, for example, link this to Asian rainfall (e.g. Wang *et al* 2017, Stephan *et al* 2019). It is less commonly studied on intraseasonal timescales—in Stephan *et al* (2019) they performed analysis on daily-mean time periods, although the purpose of their study was to analyse the effect of interannual SRP variability on its daily variability. In Ding and Wang (2007), intraseasonal variations of the Eurasian summer wave train are analysed using daily EOF analysis, and

they found that there was evidence of 'an eastward and equatorward propagation of a Rossby wave train from the northeastern Atlantic to East Asia'. However, their analysis domain is substantially larger than ours, and hence their centres of action do not align with the ones we find.

The purpose of this study is to analyse the SRP on intraseasonal timescales, by performing EOF analysis on the daily upper-level meridional winds. Following previous results at seasonal timescales, we will identify links between the intraseasonal SRP and East Asian precipitation. Furthermore, links have been made between the seasonal SRP and the location of the Mei Yu front (MYF) (Kosaka *et al* 2011), which is a summertime large-scale atmospheric front, oriented approximately zonally and which travels north across much of East Asia from April to August. On short timescales the location of the MYF can have a strong effect on Chinese rainfall (Volonté *et al* 2021, 2022), which studies of the seasonal mean will not be able to detect. Therefore, we will perform a novel investigation of whether there are links on intraseasonal timescales, determining whether there is a time-delayed or lagged relationship between the intraseasonal SRP and the location of the MYF relative to its climatological location. This will provide some evidence of short-timescale predictability between the intraseasonal SRP and East Asian weather systems, and shed light on the role of some extratropical drivers on the MYF. Recent years have seen several occurrences of extremely heavy rainfall over East Asia (e.g. Ding *et al* 2021, 2021, Volonté *et al* 2021), highlighting the need to assess the predictability of such events.

In section 2 we briefly describe the datasets and EOF analysis that we employ. In section 3, we present our findings, giving evidence for a propagating phase relationship of the intraseasonal SRP and then describing its effect on East Asian meteorology. We finish with a brief summary and discussion in section 4.

2. Data and methods

For the upper-level winds and divergence, we use the 200 hPa hourly fields from ERA5 (Hersbach *et al* 2020) for the summer months of June-July-August (JJA) over the years 1979–2020, on a horizontal resolution of 0.25°. We take four hourly fields per day at 0000, 0600, 1200 and 1800 UTC and average these to a daily field. We use the Global Precipitation Measurement (GPM) Integrated Multi-satellitE Retrievals for GPM (IMERG; Huffman *et al* 2020) dataset for precipitation observations, for JJA over 2000–2020, using the 'Final' version, which is suitable for scientific analysis.

The EOF analysis is performed on the daily 200 hPa meridional wind field from ERA5. We perform the analysis as described in Wilks (2011) and implemented by Pedregosa *et al* (2011). As in Stephan *et al* (2019), we use a domain of 30–130 °E, 20–60 °N. We also tested the analysis on the seasonal JJA-mean of the meridional wind field, which produced similar results to previous work, although we do not show the results here.

To determine the location of the MYF, we use data from the front detection algorithm developed by Volonté *et al* (2022), which is an automated algorithm based on the meridional gradient of equivalent potential temperature at 850 hPa and is designed to detect the East Asian summer monsoon front—the summertime western portion of which is the MYF. We calculate the MYF's latitudinal location over China by averaging over longitudes of 112–122 °E, and define the front as being northward or southward of its climatological position if it is over 0.75 standard deviations of its daily variability from its climatological position for the time of year. We determine the lead-lag relationship between the intraseasonal SRP and the MYF by producing a lagged contingency table (Cassou 2008, Lee *et al* 2019) based on the phases of the intraseasonal SRP and the location of the MYF relative to its climatology.

3. Results

3.1. Propagating oscillations of the intraseasonal SRP

The EOF analysis that we employ is a statistical tool that detects the principal components that explain the most variance of the analysed data. In this section, we present evidence of a phase propagation of the intraseasonal SRP, through EOF analysis of the upper-level meridional winds. This result arises as a natural interpretation of the EOF analysis; we did not specifically set out to find phase propagations. Figure 1 shows a scree plot (Wilks 2011) for the first 10 daily EOFs. It is clear that EOF1 and EOF2 explain much more variance than the remaining EOFs and notable that they explain almost identical amounts of variance. This is reminiscent of the findings of Wheeler and Hendon (2004), in which they developed a phase diagram for the MJO—i.e. there are a coupled pair of EOFs that are 'degenerate' and therefore cannot be used in isolation. We note that in Wheeler and Hendon (2004) such a pair of EOFs with almost equal explained variances indicated that the EOFs should be well suited for describing a travelling wave, and this also applies here. For seasonal EOFs (not shown), there is far greater variance explained by the first EOF (35%) than the second (15%), which indicates that only the first EOF is needed on a seasonal timescale. When analysing a larger domain that encompasses ours, Ding and Wang (2007) found that the first three EOFs are degenerate, although the difference in domains means that their

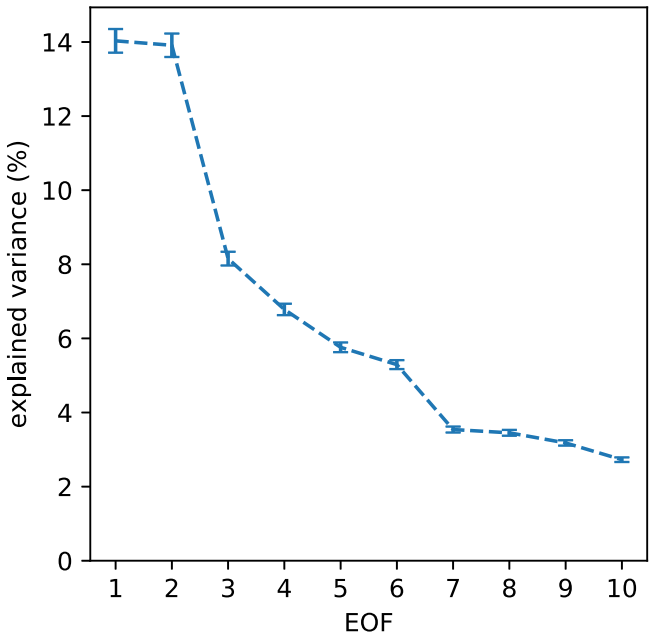

Figure 1. Scree plot of the first 10 EOFs, showing the explained variance as a percentage as well as error bars calculated as $\sqrt{\frac{2}{n}}$, where n is the number of samples (Wilks 2011, Section 12.4). This follows from considering the sampling properties of the eigenvalues under the assumptions of very large sampling size, and that their distribution is unbiased and multivariate normal. Here, we use them as a visual indicator of the expected error, noting that the first two EOFs clearly lie within their respective error bars.

centres of action are displaced from the canonical SRP centres of action. Furthermore, they found that their EOFs 2 and 3 formed an intraseasonal oscillation, which they associated with a propagating Rossby wave train.

Figure 2 shows the spatial loadings of daily EOF1 and EOF2, along with their values through a transect running approximately through their centres of action, where all values have been scaled by the standard deviation of their principal components (PCs). From figure 2(c), it is notable that the two EOFs are approximately in quadrature (i.e., $\frac{1}{4}$ of a wavelength, λ, or 90° out of phase with each other). This indicates that the first two EOFs would be well suited to representing waves of any phase or propagating waves in the upper-level meridional winds. Daily EOF1 loadings are very similar to the same for seasonal EOF1 (Stephan *et al* 2019) (note, the sign of the spatial loadings is arbitrary). EOF2 bears a strong similarity to seasonal EOF2 as well (not shown). From figure 2(c), we estimate the wavelength of EOF1 to be 52° of longitude at 36°N, or $\lambda_x = 4700$ km. EOF2 has a very similar wavelength.

Figure 3 shows Hovmöller plots for four selected years, as well as the overlayed projections of EOF 1 and 2. The years were chosen to emphasize certain features: 1980 has clear signs of an eastward-propagating oscillation from mid to late June; 1981 shows some oscillations travelling westward. 1984 and 2016are the years with strongest and weakest seasonal SRP respectively (see Stephan *et al* (2019) for 1984; 2016 not shown). We note that 2016 was a year with heavy Mei Yu rainfall, although the possible connection between this and the weaker seasonal SRP is not explored further here.

1980 shows clear signs of eastward propagation, particularly towards the end of June. This is detected by daily EOFs 1 and 2. Even when the EOF amplitudes are small (e.g. in August), there are signs of propagating oscillations. The late-June oscillation has a phase speed of approximately 5° longitude per day (at 40 °N) or approximately 5 m.s^{-1} (estimated by fitting lines to the Hovmöller diagrams). This is consistent with Hunt *et al* (2018), in which they found a phase speed propagation of 4.7 m.s^{-1} along the SWJ in winter. 1981 shows some signs of westward propagation, at the start of July, which is picked up by the EOF analysis. This appears to be a wave packet, and the EOFs are detecting its group velocity; eastward propagating features are apparent at the same time (e.g. 40–50 °E, at the start of June).

1984 has a strong positive phase of EOF1 (compare figures 2(a) with 3(c)—the spatial pattern of EOF1 is dominant) from 20 July onwards, and sporadic strong phases of EOF1 before this. There are weaker signs of propagating oscillations, e.g. around mid-July. 2016 has strong negative phase of EOF1 (see figure 2) from mid-August onwards, and some strong negative phases of EOF1 before this. Interspersed with these are clear signs of propagating oscillations. These examples illustrate that there is considerable variability in the intraseasonal SRP, and that eastward and westward propagation, as well as being stationary, are possible. Analysis of all other years (not shown) shows that eastward propagation appears to be dominant.

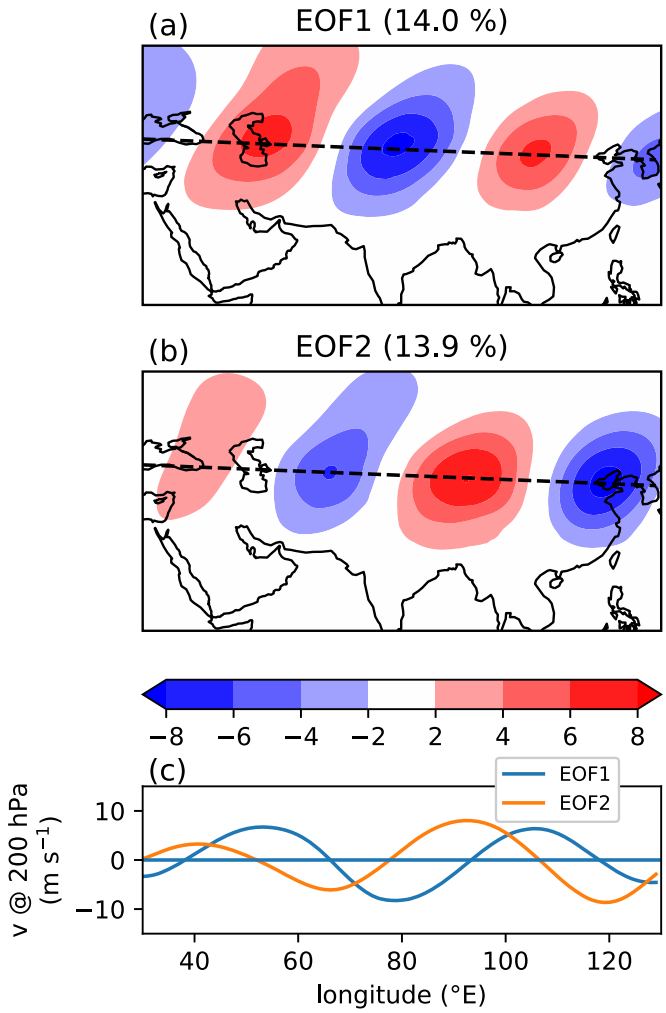

Figure 2. Spatial loadings of daily EOF1 and EOF2 (a and b), scaled by one standard deviation of their corresponding PC to have units of m.s^{-1}. The magnitude of the loadings along a transect running through their centres of action (c). The transect is shown by the dashed line in (a) and (b).

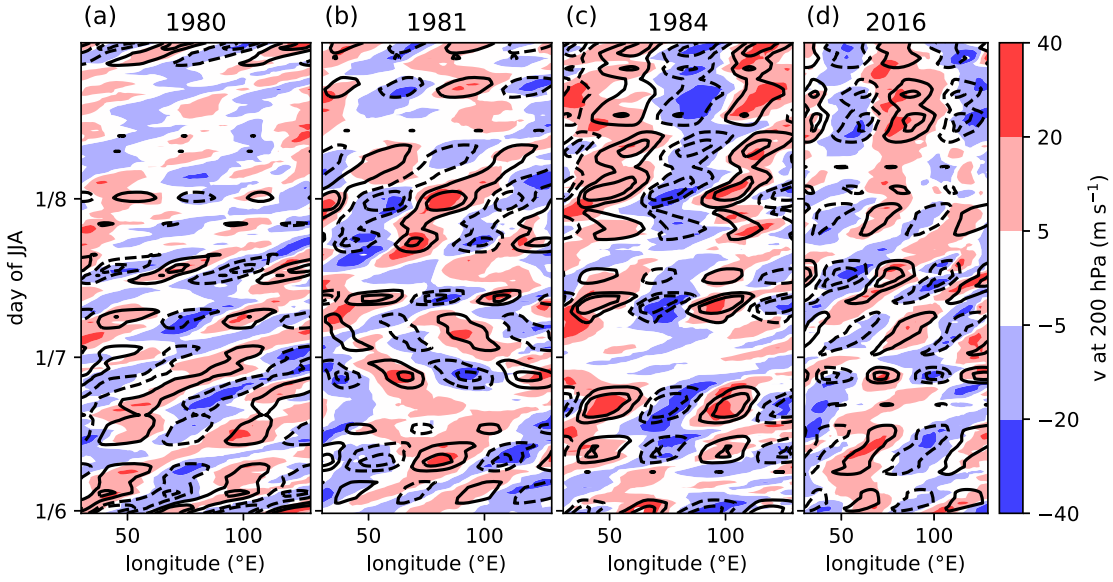

Figure 3. Hovmöller plots for four selected years showing propagation of oscillations. Anomaly of meridional wind (v) at 200 hPa along the transect shown in figure 2(a) and b is shown by red and blue coloured contours. Positive and negative phase of daily EOF1 and EOF2 are shown by solid and dashed black contours respectively, with contour levels set to ± 1 and ± 2 standard deviations.

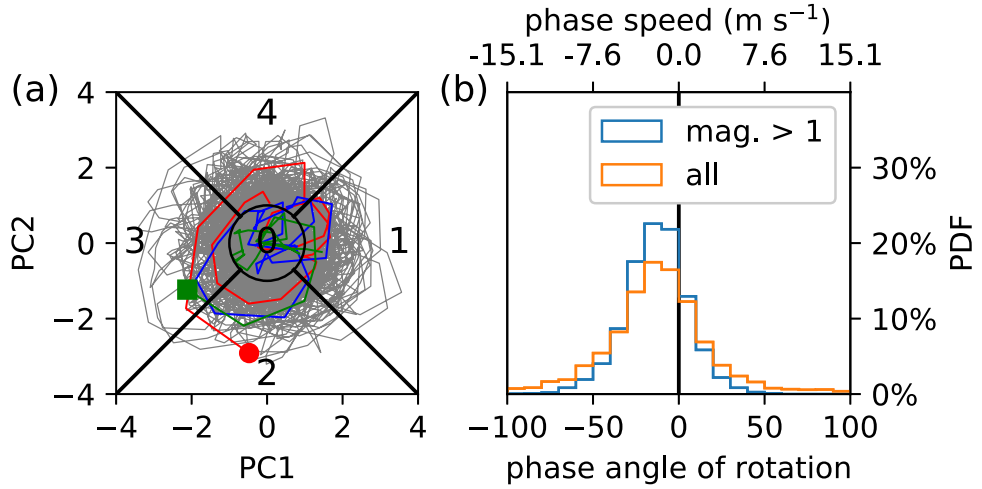

Figure 4. Phase diagram for daily EOFs 1 and 2 for all years in 1979–2020 (a), and a PDF of daily angular rotation of phase (b). For (a), all years apart from 1980are shown in grey, and 1980 is highlighted—a red circle denotes 1 June, and a green square denotes 31 August, with June, July and August shown in red, blue and green respectively. For (b), angles are binned into 10° bins and the top axis shows the equivalent phase speed calculated from a wavelength of $\lambda_x = 4677$ km determined from figure 2.

Figure 4(a) shows a phase diagram of PCs 1 and 2, in a similar manner to Wheeler and Hendon (2004). We have labelled the phases according to their location in figure 4(a): magnitude <1 is phase 0; phases 1–4 are defined where magnitude >1 and by quadrants where 1 is positive PC1, 2 is negative PC2 etc. The reason we chose to label 2 as negative PC2 is because we wished the phases 1, 2, 3, 4 to appear in succession with the dominant propagation direction, and a clockwise rotation represents an eastward propagation. The year 1980 is highlighted (also shown in figure 3); in JJA it shows a clear clockwise (eastward) propagation.

Figure 4(b) shows the distribution of angular rotation between each day—i.e., if the progression on the phase diagram is −12° (clockwise) for one day, it will contribute to the −10 to −20° bin in the density plot. Figure 4(b) shows that negative (i.e. clockwise, representing eastward propagation) rotations are more likely than positive, for both days where there is a strong combined EOF 1 and 2 and for all days. For both distributions, the mean is significantly different from zero, using a two-sided *t*-test with a 5% rejection level. For days where magnitude >1, there are approximately three times as many days where the propagation is eastward compared to westward (1490 compared to 425 days). In both cases, the modal angle is −10 to −20° (N.B. this is angle of rotation of phase per day, not longitude; conversion to degrees longitude per day or phase speed can be performed by taking the wavelength in degrees longitude or metres respectively). This corresponds to a phase speed of 1.5 m.s^{-1} to 3.0 m.s^{-1} eastward. Phase speeds of propagating waves travelling between 4.5 m.s^{-1} and 6 m.s^{-1}, i.e. including 5 m.s^{-1} as found above in the analysis of figure 3 for the propagating wave, occur 8.7% of the time when magnitude >1 and 8.2% for when magnitude <1.

Previous studies have shown that the SWJ can support Rossby waves (Enomoto *et al* 2003, Hunt *et al* 2018), and this has been postulated as an active process on the SWJ over summertime (Ding and Wang 2007, Li and Lu 2017, Wang *et al* 2017). We therefore performed analysis of the expected phase speed of the wave disturbance, assuming the wave is a Rossby wave and that the SWJ acts as a waveguide (Hoskins and Karoly 1981, Enomoto *et al* 2003). From wave theory of the linearized baratropic vorticity in the presence of a waveguide, a Rossby wave's phase velocity is given by $c_p = U - \frac{\beta_{eff}}{k^2 + l^2}$, where $\beta_{eff} = \beta - U_{yy}$, and U_{yy} is the second meridional derivative of the zonal wind (Enomoto *et al* 2003). We calculated U by taking the value of the mean zonal wind at 200hPa over the years 1979–2020 from ERA5 in the domain bounded by the contour of $U = 20$ m.s^{-1} where $U > 20$ m.s^{-1}, and likewise for U_{yy}. We estimate k from the zonal wavelength of EOFs 1 and 2: $\lambda_x = 4677$ km, giving $k = 1.34 \times 10^{-6}$ m^{-1}, and we take $l = 0$ for assumed no meridional propagation. β is calculated at 36.5 ° N. This gives a theoretical phase velocity of 0.12 m.s^{-1}, which is lower than the observed value here for the detected propagating wave. However, it is close to the value derived from the mode of the rotation angles in figure 4, and is well within the uncertainty defined by the half-width of the PDF. Thus, this provides limited evidence that the daily EOF analysis could be detecting the phase of propagating Rossby waves formed in the SWJ waveguide.

3.2. SWJ and East Asian precipitation conditional on phase of the intraseasonal SRP

We have identified that the intraseasonal SRP can have different phases. Here, we ascertain the effect of these phases on East Asian precipitation patterns. Figure 5 shows precipitation and upper-level winds conditional on

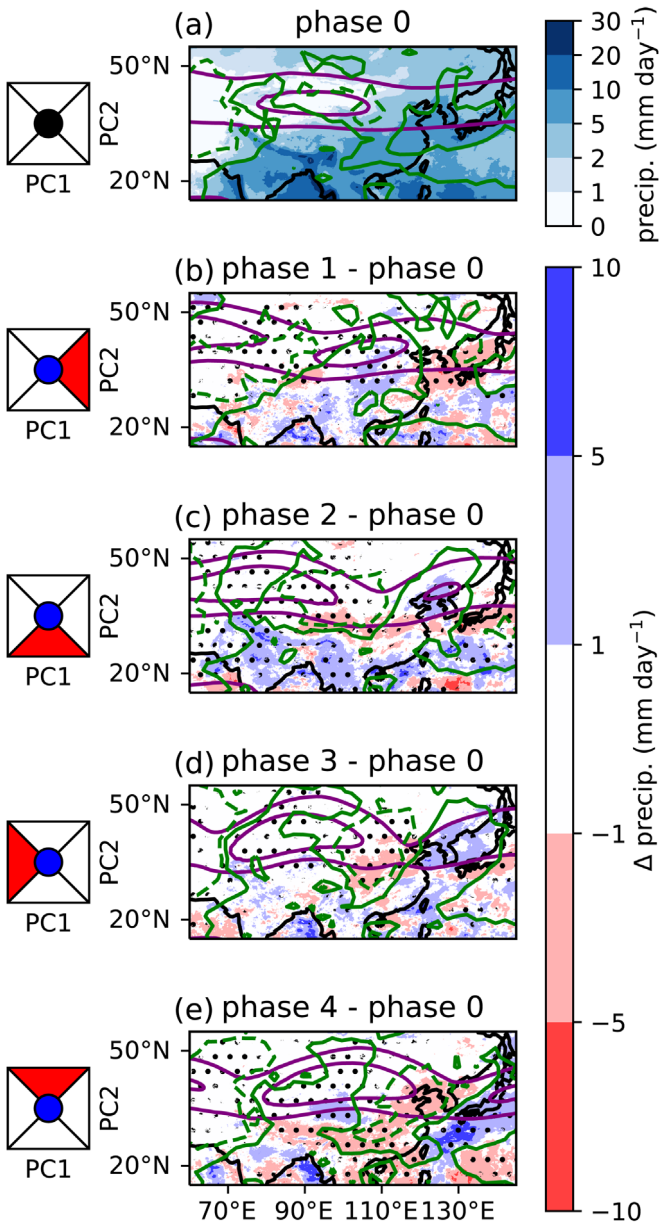

Figure 5. East Asian precipitation, SWJ and upper-level divergence conditional on the phase of daily EOFs 1 and 2. Left column shows how each composite precipitation field was calculated: (a) was the mean over all points in phase 0 (i.e. magnitude < 1), and (b)–(e) show the difference between the phase in question (shown by red in left column) and phase 0 (shown by blue). For (b)–(e), coloured contours show precipitation differences, with statistically significant differences shown by stippling using a two-sided Wilcoxon-Mann-Whitney rank-sum test with a 2% rejection level (Wilks 2011, pp. 159–161). Purple lines show the position of the SWJ, using 200 hPa wind speeds contoured at 20 and 30 m.s^{-1}. Green solid and dashed lines show regions of upper-level (200 hPa) divergence and convergence respectively, with values of absolute magnitude exceeding 1×10^{-6} s^{-1} shown. The divergence field was smoothed using averaging over 10×10 grid boxes (with a horizontal grid length of 0.25°) to remove some of its noise.

the phase of the daily EOFs 1 and 2. Phase 0, corresponding to when there is little intraseasonal SRP activity, is close to the mean over the given period from 2000–2020 (not shown), and shows prominent features such as heavy rainfall over the coast of Myanmar, the Western Ghats in India and the Himalayas, associated with the Indian summer monsoon. Associated with the East Asian summer monsoon, large areas of rainfall are present over China, although the rainfall is lighter than the heavier rainfall caused by the Indian summer monsoon.

For the SWJ, a trough progressing eastward is clear during phases 1–4, centred over approximately 90 °E, 110 °E, 120 °E and 130 °E respectively. These longitudes correspond to the locations of the EOF spatial loadings in figure 2. The trough is associated with a region of upper-level convergence upstream (west) and divergence downstream (east). These are likely due to ageostrophic effects at the jet exit and entrance regions respectively. Upper-level convergence is associated with subsidence. Correspondingly, these are regions of negative rainfall anomaly (e.g. phase 4 over China and the Yellow Sea). Conversely, regions of divergence are associated with

upward motion, which is co-located with areas of heavier rainfall (e.g. phase 3 over the Yellow Sea and the Korean Peninsula).

Each phase shows a distinct pattern of rainfall from phase 0 (significant at a 2% level, using a Wilcoxon-Mann-Whitney test, unless indicated). Some notable features are that phase 1 has more precipitation over large regions of inland China, including the Yangtze river basin (YRB). Li and Lu (2017) also found connections between YRB rainfall anomaly and the meridional anomalies of the jet, however their analysis was performed on monthly data and so they were investigating the same phenomenon on a different timescale. Phase 2 has higher rainfall over the western end of the Himalayas, and the Yellow Sea and Korean Peninsula. Phase 3 has again higher rainfall over the Yellow Sea and the Korean Peninsula, as well as over the Sea of Japan, although these are not statistically significant. Phase 3 also has lower rainfall over inland China. Phase 4 has a large dry anomaly over China, and a very large and strong wet anomaly over the Philippine Sea. Phase 4 shows increased rainfall over the Tibetan Plateau. This is consistent with Wang *et al* (2018), who show a filtered upper-level geopotential height anomaly which is equivalent to our phase 4 (compare their figure 2(a) and figure 2(a) above). Thus, the phase of the intraseasonal SRP is a driver of East Asian rainfall when analysed over multiple years, and a plausible mechanism—the upper-level convergence and divergence driving large-scale descent and ascent respectively—linking the two has been established.

To further explore the mechanism, figure 6 shows vertical cross sections over the region roughly aligned with the trough in figure 5(d) (phase 3) averaged over 120–130 °E. This region encompasses the Yellow Sea (33–40 ° N), which we will focus on here. The dry and wet anomalies in the Yellow Sea seen in figure 5 are clearly visible. The dry anomalies can be seen in phase 1 between 28–39 °N and phase 4 between 34–43 °N. The wet anomalies are evident in phase 2 between 35–45 °N and phase 3 between 33–43 °N. The maximum dry anomaly is approximately a factor of 2 smaller, and the maximum wet anomaly is approximately 50% larger than the precipitation in phase 0. The dry anomaly is associated with weaker (phase 1) or even negative (phase 4) vertical motion, and the wet anomaly is associated with stronger than phase 0 vertical motion. Both dry anomalies are associated with upper-level convergence, consistent with our hypothesized mechanism, although this is weak for phase 1. For both wet anomalies, there is substantial divergence aloft.

The position of the SWJ varies across the different phases, although the stronger 20 $m.s^{-1}$ contour does not show a great degree of movement on its southern edge. The SWJ maxima in phases 1 and 2 are 5° further north than for phases 3 and 4. The northern edges of both contours shows a clear progression through the phases, with maximum extent at phase 1 and minimum at phase 3, consistent with figure 5. The location of the downward vertical winds and upper level convergence is clearest in phase 4, and is consistent with the trough being located further east than the cross-section domain and our proposed mechanism.

Further south of the Yellow Sea, phase 4 shows a very strong wet anomaly from 20–31 °N, with a maximum anomaly being approximately twice as large as the phase 0 precipitation. This is associated with stronger than phase 0 (or any other phase) updraughts at around 500 hPa for this region. The circulation appears to be associated with an overturning circulation that extends further south than 20 °N, and so outside our analysis domain. This could occur because the intertropical convergence zone (ITCZ) extends further northwards in this phase, leading to ascent in our domain and divergence aloft.

3.3. Lagged location of MYF conditional on phase of the intraseasonal SRP

Given the evidence for a propagating intraseasonal SRP phase and its effect on East Asian precipitation, we wish to see whether we can link the intraseasonal SRP phase to the MYF, a dominant mode of East Asian summer atmospheric variability. Additional motivation for this analysis is provided by the result of Volonté *et al* (2022), who showed that the location of the MYF was influenced by the SWJ on a seasonal scale, and hence investigating their interaction on shorter timescales might help to shed light on the mechanisms of this. We consider the location of the MYF relative to its climatology at a lagged number of days after a particular intraseasonal SRP phase. Figure 7 shows a lagged contingency plot of the location of the MYF relative to its climatological location for each phase of the intraseasonal SRP, as in Cassou (2008) and Lee *et al* (2019). This is calculated by using an index of each phase of the intraseasonal SRP, the leading variable, and comparing this with the index of the MYF location for different lags. As described in section 2, we define three possibilities for the location of the MYF—northward, southward and close to climatology —only the first two are shown. Two statistical significance tests must be met for the bars to be shaded: a χ^2 test on the distributions being significantly different at the 99% significance level, and a Gaussian normal test on the value being significantly different from 0% at a 95% significance level (Cassou 2008).

Two intraseasonal SRP phases stand out as having strong, statistically significant effects on the northward relative location of the MYF — 2 and 4. 3–10 days after the occurrence of phase 2, the front is significantly less likely to be northward of its climatological location (left column). In phase 4, from days 3–8, the front is significantly more likely to be northward of its climatological location (left column). Note, it is possible for an individual lag to be more likely for both northward and southward—it implies that it is less likely to be close to its

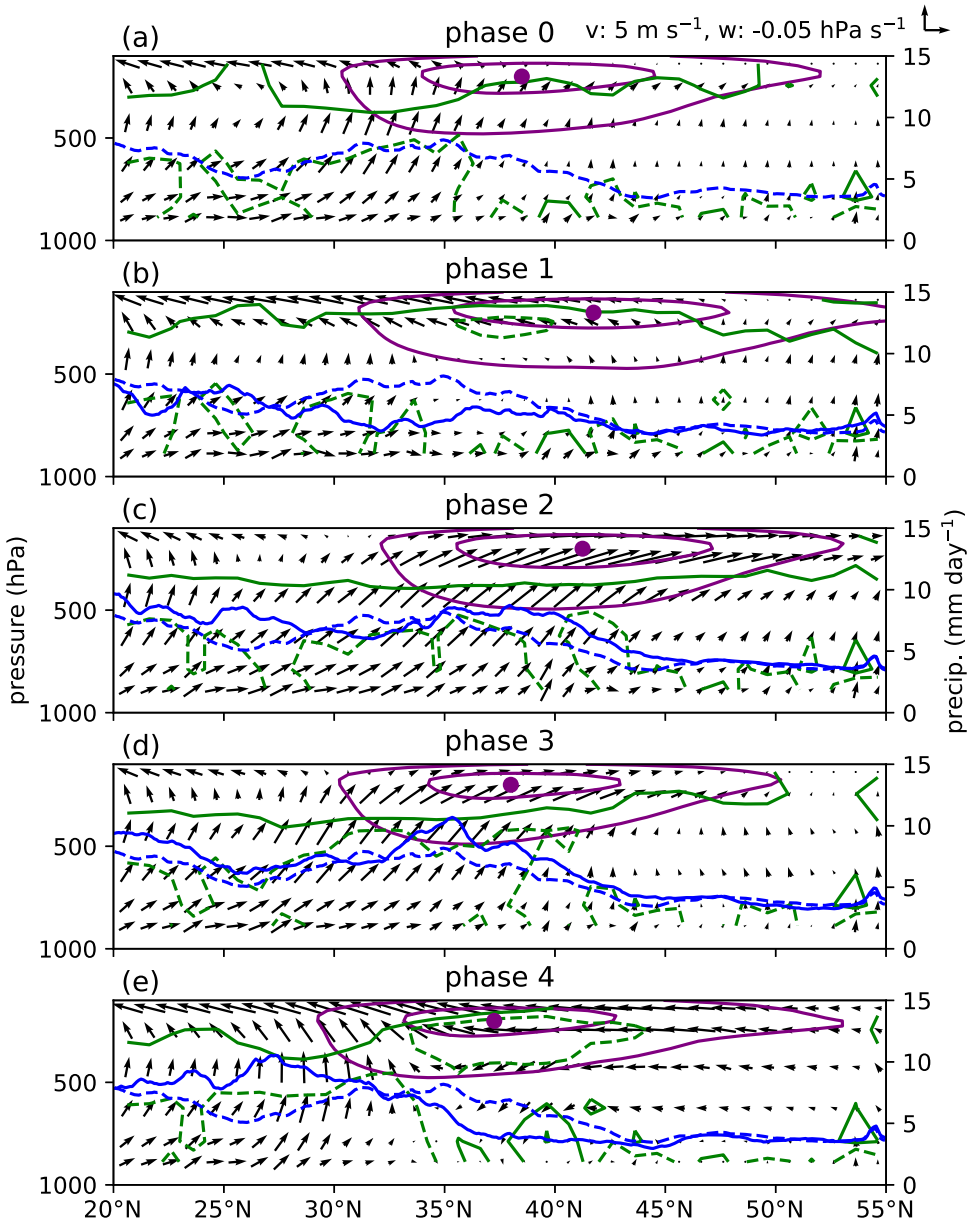

Figure 6. Vertical cross section showing the SWJ, meridional and vertical wind, divergence and precipitation conditional on the phase of daily EOFs 1 and 2, averaged over 120–130 °E. Purple lines show SWJ contoured at 10 and 20 m.s^{-1}, and the purple circle shows the position of the maximum. Arrows show the meridional (v) and vertical (w) wind (scale top right). Green solid and dashed lines show divergence and convergence respectively, with values of absolute magnitude exceeding 5×10^{-7} s^{-1} shown. Blue dashed line shows the precipitation for phase 0 in all panels, and blue solid lines shows the precipitation conditional on phase for (b)–(e).

climatological location (not shown). In both cases, the MYF returns to its climatological location after 8 or 10 days.

Two possibilities suggest themselves for the approximately 3-day delay. The first is that, because of the eastward propagating nature of the some intraseasonal SRP waves, e.g. 3 days after phase 2, its trough and upper-level divergence wind patterns are affecting the location of the MYF. For example, it could be that the location of the upper-level convergence (figure 5) is driving subsidence that causes lower-level divergence, which in turn means the MYF is less likely to be relatively further north. The second is that, because the SWJ is further north than the MYF, any effects (such as the one just mentioned) take time to influence the front. It could also be a combination of the above; further investigation on this point is needed in a future study.

4. Summary and discussion

Daily EOF analysis of the meridional winds at 200 hPa taken from ERA5 was performed, and we linked the phase of the propagating features to East Asian precipitation patterns and the location of the Mei Yu front (MYF).

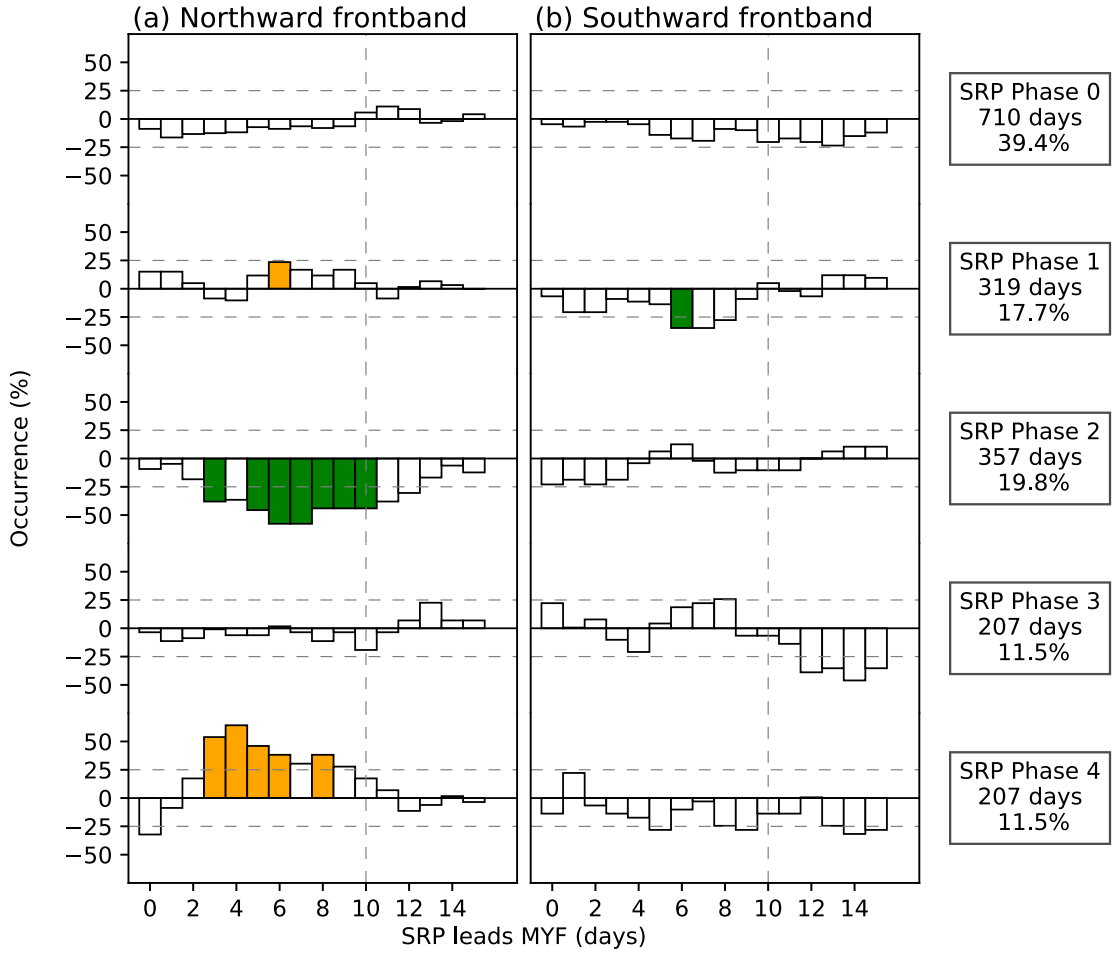

Figure 7. Contingency plot of relative occurrence of anomalous (a) northward or (b) southward MYF location as a function of lag time following the intraseasonal SRP phase, after Cassou (2008) and Lee *et al* (2019). Green and yellow shading shows significant positive and negative relationships respectively, where significance is determined by applying a χ^2 test on the distribution and a Gaussian normal test on the value difference from 0% occurrence. Dashed lines are shown to aid visualization but do not denote significance.

From the EOF analysis, we presented compelling evidence for the intraseasonal SRP being a natural mode of variability of the SWJ. The daily EOF analysis naturally determined that two EOFs were needed to describe the upper-level meridional winds, indicating that the phase of the oscillation can take any value and all phases are equivalently likely, as would be caused by a propagating wave. Daily EOF1 bears a strong resemblance to seasonal EOF1 from previous studies. Propagating waves were also found to be common. The modal direction of propagation is eastward, and the phase speed of propagating oscillations is approximately 5 $m.s^{-1}$ eastward. Using wave analysis based on linearized baratropic vorticity and SWJ waveguide theory, we presented limited evidence that the waves are possibly Rossby waves.

The intraseasonal SRP has an effect on the upper-level divergence, through local jet entrance and exit regions, and ageostrophic dynamics. It consequently has an effect on East Asian precipitation patterns through induced subsidence and upward motion of air. Some of the prominent precipitation signals are: wet anomalies over inland China for phase 1; wet anomalies over the western Himalayas, Yellow Sea and Korean Peninsula for phase 2; wet anomalies over the Yellow Sea, Korean Peninsula and Sea of Japan for phase 3; and strong wet anomalies over Philippine Sea for phase 4. Thus, the phase of the wave is seen to be important for East Asian precipitation patterns. With a focus on the Yellow Sea, the wet and dry anomalies over this region were found to be closely related to the phase of the intraseasonal SRP, and the associated circulation patterns and upper-level convergence and divergence.

We found some signs of predictability: the lagged relationship between the intraseasonal SRP phase and relative location of MYF indicate that the MYF is partially controlled by extratropical drivers. In particular, phase 4 leads relative northward location of the MYF by 3–8 days. Furthermore, the propagation of waves indicates that there may be another source of predictability; if a propagating wave is detected, and there is a known response to a later phase of the wave, then a few days later this response may be predicted, although this was not explored further here.

Our work here shows that the phase of waves on the SWJ is important for East Asian meteorology. This differs from previous work, in which the phase is assumed to be stationary or quasi-stationary (Enomoto *et al* 2003, Stephan *et al* 2019), and the important aspect was taken as being the group velocity of the waves in those studies. Undoubtedly the group velocity is important, as this determines the energy transport by the wave, but here we show that so too is its phase, and that daily EOF analysis provides a simple means of diagnosing this wave activity. Furthermore, it is interesting to note that the first two EOFs of the intraseasonal SRP correspond to the first two EOFs of the seasonal SRP, but that the explained variance of these is the same for the intraseasonal SRP and not for the seasonal. This indicates that there is a mechanism that acts to anchor the intraseasonal SRP in the location where it appears on seasonal timescales, such as perhaps anchoring due to orography or anchoring arising due to the location of whatever is generating variability in the intraseasonal SRP. Such a mechanism would be a good candidate for future study. One way of investigating this could be to perform low-pass filtering on the intraseasonal SRP with different thresholds for the cut-off frequency, to see how the intraseasonal and seasonal SRPs are related.

We calculated the theoretical phase speed of the waves above from the mean fields describing the SWJ. It would be possible to perform a similar calculation on the daily fields, and relate this to the observed phase change of the intraseasonal SRP. The hypothesis would be that, as the SWJ strengthened, the phase speed of the waves would increase, and so one would expect to see a propagating wave under these circumstances. We made some attempt to perform this analysis (not shown), but the results were inconclusive and showed little correlation between the theoretical and observed phase speed. Refinement of this technique could provide the basis of interesting future work and lead to another source of predictability of East Asian precipitation.

Here, we analysed waves on the SWJ without determining what excited them. It would be of great interest to see what effect large-scale drivers of East Asian weather had on the intraseasonal SRP; drivers that have been shown to affect the seasonal SRP include Indian summer monsoon (Beverley *et al* 2021) and the North Atlantic oscillation (Liu *et al* 2020). This could further increase the predictability window of East Asian meteorology, and the intraseasonal SRP as introduced here provides a metric for evaluating medium-range to seasonal forecasts.

Finally, our work here has been based on reanalysis and observations. Evaluating the intraseasonal SRP in atmospheric models could determine whether they realistically represent the relevant processes, and if they correctly reproduce the effects on East Asian meteorology. High-resolution simulations struggle to properly represent East Asian precipitation (Muetzelfeldt *et al* 2020), and this could be, in part, due to their failure to correctly represent the large-scale drivers, such as the phase of the intraseasonal SRP.

Acknowledgments

MM, RS, AGT, PLV and AM were supported by the COSMIC project through the Met Office Climate Science for Service Partnership (CSSP) China as part of the Newton Fund, contract number P106301.

We would like to acknowledge Robert Lee for providing us with an example of his code for producing lagged contingency tables, which we modified here.

Data availability statement

The data that support the findings of this study are available upon reasonable request from the authors.

ORCID iDs

Mark R Muetzelfeldt https://orcid.org/0000-0002-6851-7351

References

Beverley J D, Woolnough S J, Baker L H, Johnson S J, Weisheimer A and O'Reilly C H 2021 Dynamical mechanisms linking Indian monsoon precipitation and the circumglobal teleconnection *Clim. Dyn.* **57** 2615–36

Cassou C 2008 Intraseasonal interaction between the madden-julian oscillation and the north atlantic oscillation *Nature* **455** 523–7

Ding L, Li T and Sun Y 2021 Subseasonal and synoptic variabilities of precipitation over the yangtze river basin in the summer of 2020 *Adv. Atmos. Sci.* **38** 2108–24

Ding Q and Wang B 2005 Circumglobal teleconnection in the Northern Hemisphere summer *J. Clim.* **18** 3483–505

Ding Q and Wang B 2007 Intraseasonal teleconnection between the summer Eurasian wave train and the Indian monsoon *J. Clim.* **20** 3751–67

Ding Y, Liu Y and Hu Z-Z 2021 The record-breaking mei-yu in 2020 and associated atmospheric circulation and tropical SST anomalies *Adv. Atmos. Sci.* **38** 1980–93

Enomoto T, Hoskins B J and Matsuda Y 2003 The formation mechanism of the Bonin high in August *Q. J. R. Meteorolog. Soc.* **129** 157–78

Hersbach H *et al* 2020 The ERA5 global reanalysis *Q. J. R. Meteorolog. Soc.* **146** 1999–2049

Hoskins B J and Karoly D J 1981 The steady linear response of a spherical atmosphere to thermal and orographic forcing *J. Atmospheric Sci.* **38** 1179–96

Huffman G J *et al* 2020 Integrated MultisatellitE Retrievals for GPM (IMERG) technical documentation *NASA/GSFC Code* **612** 47 (https://docserver.gesdisc.eosdis.nasa.gov/public/project/GPM/IMERG_doc.06.pdf)

Hunt K M R, Turner A G and Shaffrey L C 2018 Extreme daily rainfall in Pakistan and north India: Scale interactions, mechanisms, and precursors *Mon. Weather Rev.* **146** 1005–22

Kosaka Y, Xie S-P and Nakamura H 2011 Dynamics of interannual variability in summer precipitation over East Asia *J. Clim.* **24** 5435–53

Lee R W, Woolnough S J, Charlton-Perez A J and Vitart F 2019 ENSO modulation of MJO teleconnections to the North Atlantic and Europe *Geophys. Res. Lett.* **46** 13535–45

Li X and Lu R 2017 Extratropical factors affecting the variability in summer precipitation over the Yangtze River basin, China *J. Clim.* **30** 8357–74

Liu B, Yan Y, Zhu C, Ma S and Li J 2020 Record-breaking Meiyu rainfall around the Yangtze River in 2020 regulated by the subseasonal phase transition of the North Atlantic Oscillation *Geophys. Res. Lett.* **47** e2020GL090342

Muetzelfeldt M R, Schiemann R, Turner A G, Klingaman N P, Vidale P L and Roberts M J 2020 Evaluation of Asian summer precipitation in different configurations of a high-resolution GCM at a range of decision-relevant spatial scales *Hydrology and Earth System Science* **25** 6381–405

Pedregosa F *et al* 2011 Scikit-learn: Machine Learning in Python *J. Machine Learning Research* **12** 2825–30

Stephan C C, Klingaman N P and Turner A G 2019 A mechanism for the recently increased interdecadal variability of the Silk Road pattern *J. Clim.* **32** 717–36

Stephan C C, Ng Y H and Klingaman N P 2018 On Northern Hemisphere wave patterns associated with winter rainfall events in China *Adv. Atmos. Sci.* **35** 1021–34

Volonté A, Muetzelfeldt M R, Schiemann R, Turner A G and Klingaman N P 2021 Magnitude, scale, and dynamics of the 2020 Mei Yu rains and floods over China *Adv. Atmos. Sci.* **38** 2082–96

Volonté A, Turner A G, Schiemann R, Vidale P L and Klingaman N P 2022 Characterising the interaction of tropical and extratropical air masses controlling East Asian summer monsoon progression using a novel frontal detection approach *Weather and Climate Dynamics* **3** 575–99

Wang L, Xu P, Chen W and Liu Y 2017 Interdecadal variations of the Silk Road pattern *J. Clim.* **30** 9915–32

Wang M, Wang J, Duan A, Liu Y and Zhou S 2018 Coupling of the quasi-biweekly oscillation of the Tibetan Plateau summer monsoon with the Arctic oscillation *Geophys. Res. Lett.* **45** 7756–64

Wheeler M C and Hendon H H 2004 An all-season real-time multivariate MJO index: Development of an index for monitoring and prediction *Mon. Weather Rev.* **132** 1917–32

Wilks D S 2011 *Statistical Methods in the Atmospheric Sciences* (Elsevier: Academic Press) 3rd edn p 676

Yasui S and Watanabe M 2010 Forcing processes of the summertime circumglobal teleconnection pattern in a dry AGCM *J. Clim.* **23** 2093–114